THE JOURNAL OF
PHYSICAL CHEMISTRY A
Article
pubs.acs.org/JPCA

Optical Emission from Microwave Activated C/H/O Gas Mixtures for Diamond Chemical Vapor Deposition

James C. Richley, Mark W. Kelly, and Michael N. R. Ashfold*

School of Chemistry, University of Bristol, Bristol BS8 1TS, U.K.

Yuri A. Mankelevich

Skobel'tsyn Institute of Nuclear Physics, Moscow State University, Leninskie Gory, Moscow 119991, Russia

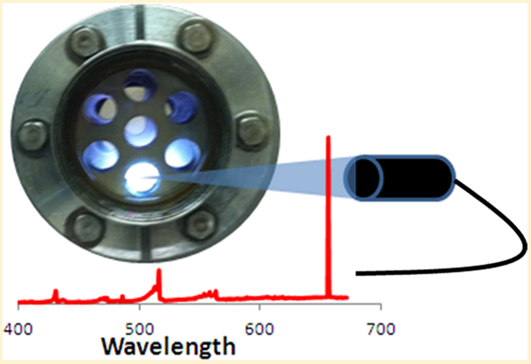

ABSTRACT: The spatial distributions and relative abundances of electronically excited H atoms, OH, CH, C_2 and C_3 radicals, and CO molecules in microwave (MW) activated $CH_4/CO_2/H_2$ and CO/H_2 gas mixtures operating under conditions appropriate for diamond growth by MW plasma enhanced chemical vapor deposition (CVD) have been investigated by optical emission spectroscopy (OES) as a function of process conditions (gas mixing ratio, incident MW power, and pressure) and rationalized by reference to extensive 2-dimensional plasma modeling. The OES measurements clearly reveal the switch in plasma chemistry and composition that occurs upon changing from oxygen-rich to carbon-rich source gas mixtures, complementing spatially resolved absorption measurements under identical plasma conditions (Kelly et al., companion article). Interpretation of OES data typically assumes that electron impact excitation (EIE) is the dominant route to forming the emitting species of interest. The present study identifies a number of factors that complicate the use of OES for monitoring C/H/O plasmas. The OH* emission from EIE of ground state OH(X) radicals can be enhanced by excitation energy transfer from metastable $CO(a^3\Pi)$ molecules. The CH* and C_2* emissions can be boosted by chemiluminescent reactions between, for example, C_2H radicals and O atoms, or C atoms and CH radicals. Additionally, the EIE efficiency of each of these radical species is sensitively dependent on any spatial mismatch between the regions of maximal radical and electron density, which itself is a sensitive function of elemental C/O ratio in the process gas mixture (particularly when close to 1:1, as required for diamond growth) and the H_2 mole fraction.

1. INTRODUCTION

The companion article[1] reported detailed 2-dimensional (2-D) modeling of the plasma chemistry and composition in microwave activated C/H/O gas mixtures used for growth of polycrystalline diamond films by chemical vapor deposition (CVD). The model was tensioned and validated by comparison with spatially resolved measurements of the absolute column densities of selected transient species in the hot plasma region of both $CH_4/CO_2/H_2$ and CO/H_2 gas mixtures, as functions of process conditions. Such measurements are essential for detailed understanding of the plasma chemistry and for CVD process optimization but require specialist diagnostic expertise. Optical emission spectroscopy (OES) is an alternative, noninvasive, and sensitive technique that is simple to implement and thus finds widespread use as a means of monitoring specific (emitting) species in a wide range of plasma environments, including those used in diamond CVD. Reliable interpretation of OES data does, however, require a proper understanding of the excitation and de-excitation processes for the emitting species of interest. Given such knowledge, careful analysis can yield detailed information about quantities like relative number densities, local gas and electron temperatures, etc., as demonstrated in the context of diamond CVD for the case of microwave (MW) activated hydrocarbon/H_2 gas mixtures (with or without added Ar).[2−7] Comparisons between spatially resolved relative emission intensities from electronically excited C_2, CH, H($n > 2$), H_2, and Ar species (as revealed by OES) and absolute column densities of C_2, CH, and H($n = 2$) species measured in absorption (by cavity ring down spectroscopy (CRDS)) in MW-activated $CH_4/H_2/Ar$ gas mixtures reveal many parallels. The monitored emitters were found to partition into two groups, reflecting the chemistry that underpins their generation. Companion modeling confirmed that the distributions of emitting species like Ar(4p), $H_2(3p,{}^3\Sigma_u{}^+)$, and H(n = 3, 4) atoms are determined primarily by electron impact excitation (EIE), whereas thermally driven chemistry has a much greater influence on the distributions of emitting C_2 and CH radicals.[6] Notwithstanding the recognized limitations of OES as a method for investigating ground state species, the consensus view is that careful OES measurements

Received: June 23, 2012
Revised: August 15, 2012
Published: August 17, 2012

can offer a relatively straightforward, low cost route to monitoring C/H/(Ar) plasmas under conditions such as those typically used in the CVD of polycrystalline (and single crystal) diamond.[5−7]

The present study extends this comparison to the case of C/H/O plasmas. These have been proposed[8−15] as a route to growing diamond at lower substrate temperatures (T_{sub}) than with the traditional C/H gas mixtures (with or without some added Ar). The companion article[1] presents the first quantitative diagnosis of the chemistry and composition of $CH_4/CO_2/H_2$ plasmas under conditions relevant to contemporary diamond CVD. Here, we survey the utility of careful, spatially resolved OES measurements for monitoring C/H/O plasmas and highlight the potential complications that can arise if the species of interest and the electrons have very different spatial distributions or if the intensity of chemiluminescent emission from products of exothermic reactions in the plasma becomes comparable to that from EIE processes. Previous analyses of spatially resolved B and, particularly, BH emission intensities in B/H/Ar plasmas[16] are also reappraised in the light of the present findings.

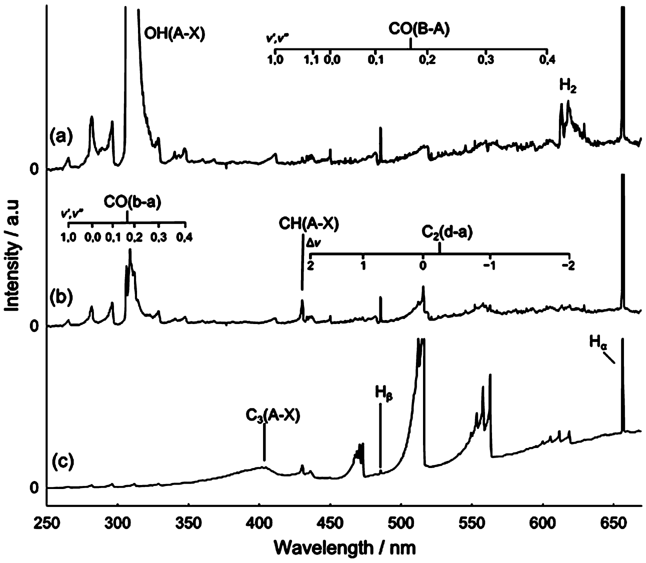

Figure 1. Optical emission spectra from $CH_4/CO_2/H_2$ plasmas with $X_{C/\Sigma}$ = (a) 0.46, (b) 0.495, and (c) 0.54 and $X_0(H_2) = 0.3$, measured at z = 10 mm, across the wavelength range 250−700 nm. The monochromator/CCD assembly only allowed accumulation of spectra in a 300 nm bandwidth, so the displayed spectra each involve two data sets. Relative intensities in the three spectra measured at any given wavelength are directly comparable, but the data has not been corrected for any wavelength dependence in the detection sensitivity.

2. EXPERIMENTAL SECTION

The MW PECVD reactor and the methodology for spatially resolved OES measurements as a function of height (z) above the substrate have been described previously.[6,17] The light collection efficiency was enhanced by use of a two lens telescope (objective lens, with focal length f = 14 cm, plus an eyepiece (f = 7 cm)) with an aperture positioned in the image plane of the former to project emission from a user selected height z within the core of the plasma ball (above the substrate center) onto one end of a multicore quartz optical fiber. The light exits the fiber as a vertical stripe and is dispersed through a small monochromator equipped with a charge coupled device (CCD) strip detector, providing a spectral resolution <1 nm.

As in the companion work,[1] base conditions for the $CH_4/CO_2/H_2$ plasma were chosen as total pressure, p = 150 Torr; input power, P = 1 kW; and input flow rates $F(CH_4) = F(CO_2)$ = 175 standard cm^3 per minute (sccm), $F(H_2)$ = 150 sccm. Again, we adopt the Bachmann notation[18] by defining the ratio $X_{C/\Sigma} = X_{elem}(C)/[X_{elem}(C) + X_{elem}(O)]$ in the source gas mixture, where $X_{elem}(C)$ and $X_{elem}(O)$ are the elemental carbon and oxygen mole fractions. Base conditions thus correspond to $X_{C/\Sigma} = 0.5$ with an H_2 input mole fraction, $X_0(H_2) = 0.3$. When changing one discharge parameter, all others were maintained at their base values except when investigating the effect of varying the respective gas flow rates. Effects of changing $X_{C/\Sigma}$ at a given $X_0(H_2)$ were studied by varying $F(CH_4)$ to compensate for any change in $F(CO_2)$, while the effect of varying $X_0(H_2)$ was explored by holding $X_{C/\Sigma}$ fixed and adjusting $\{F(CH_4) + F(CO_2)\}$ to counteract any change in $F(H_2)$. Again, as previously,[1] it proved informative to study the equivalent (in terms of C and O fraction) CO/H_2 plasma. Base conditions in this case comprised $F(CO)$ = 206 sccm, $F(H_2)$ = 294 sccm (i.e. $X_0(CO) = 0.412$, $X_0(H_2) = 0.588$), p = 150 Torr, and P = 1 kW. It was possible to raise $X_{C/\Sigma} > 0.5$ in this case by progressive replacement of CO by CH_4 in the input gas mixture.

3. RESULTS AND DISCUSSION

3.1. Optical Emission from $CH_4/CO_2/H_2$ Plasmas at Different $X_{C/\Sigma}$, with $X_0(H_2) = 0.3$; Spectra and Spatial Profiles.

Figure 1 shows optical emission spectra from the center of the hot region (z = 10 mm) of $CH_4/CO_2/H_2$ plasmas with $X_{C/\Sigma}$ = 0.46, 0.495, and 0.54, $X_0(H_2) = 0.3$, and all other parameters held at the base values. Features to note include the H Balmer-α and Balmer-β lines, the $H_2(3p^3\Sigma_u^+-2s^3\Sigma_g^+)$ Fulcher band at ∼602 nm, the $C_2(d^3\Pi-a^3\Pi)$ Swan bands centered ∼515 nm, broad $C_3(A^1\Pi_u-X^1\Sigma_g^+)$ emission around 405 nm, $CH(A^2\Delta-X^2\Pi)$ emission at ∼431 nm, the OH-$(A^2\Sigma^+-X^2\Pi)$ origin band at ∼308 nm, and two sets of emissions attributable to electronically excited CO molecules (the $B^1\Sigma^+-A^1\Pi$ (Ångstrom) and $b^3\Sigma^+-a^3\Pi$ (3rd positive) systems, spanning the respective wavelength ranges ∼420−600 nm and ∼260−340 nm). Henceforth, it will prove convenient to refer to these emitters simply as H*, H_2*, C_2*, etc. Even a cursory inspection is sufficient to show that the relative intensities of these features are sensitive to $X_{C/\Sigma}$; the relative intensities of the CH* and, particularly, the C_2* and C_3* emissions increase dramatically as $X_{C/\Sigma}$ is raised from 0.46 to 0.54, while the OH* emission shows the opposite behavior. This latter trend accounts for the choice of $X_{C/\Sigma} = 0.495$ rather than 0.5. As Figure 1 shows, the OH* feature is heavily overlapped by the $v' = 0 - v'' = 2$ band of the CO(b−a) system. The two features have very different spectral band contours, which aid deconvolution, but the presence of the CO* emission limits our ultimate sensitivity to OH*. $X_{C/\Sigma} = 0.495$ thus represents a good compromise under which conditions we can trace the variation of OH*, CH*, and C_2* emissions with changes in process parameters.

Prior to a more quantitative description of these trends with $X_{C/\Sigma}$, we first consider the spatial profiles of the various emitters. Figure 2 shows the measured z-dependence of the relative emission intensities of these species, again for $X_{C/\Sigma}$ = 0.46, 0.495, and 0.54 and $X_0(H_2) = 0.3$. The peak emission intensity for each species, in each plot, has been normalized to unity. The CO* emission consistently peaks at the smallest z

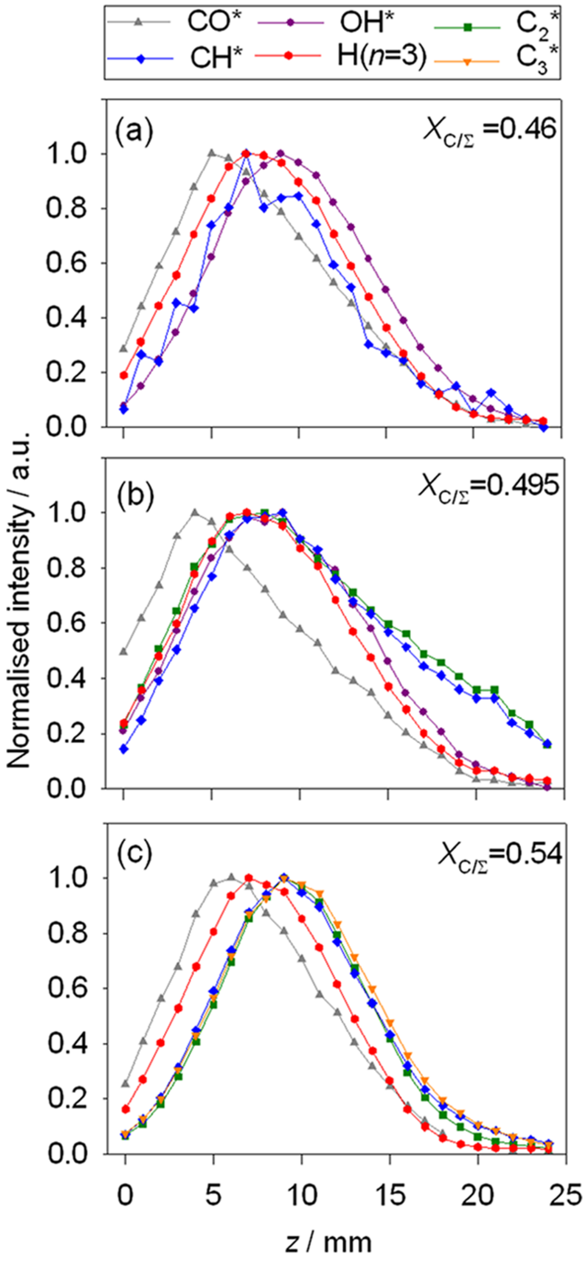

Figure 2. Spatial profiles (intensity versus z) of the H(n = 3)*, CO*, and, where appropriate, OH*, CH*, C_2*, and C_3* emissions measured for $CH_4/CO_2/H_2$ plasmas with $X_0(H_2) = 0.3$ and $X_{C/\Sigma}$ = (a) 0.46, (b) 0.495, and (c) 0.54. The peak intensity of each emitter in each plot has been scaled to unity.

(∼5 mm), followed by the H* emissions, which maximize at $z \approx 7.5$ mm. The radical emissions always peak at larger z: OH* at $z \approx 9$ mm when $X_{C/\Sigma} = 0.46$, and CH*, C_2*, and C_3* at $z \approx 9$ mm when $X_{C/\Sigma} = 0.54$. This can be understood as follows. The principal route to electronically excited species in MW-activated plasmas at these pressures is EIE of the corresponding ground (or, in the case of C_2, low lying excited) state species. The spatial distributions of CO*, H*, and the various radical species (e.g., OH*) should thus reflect the convolution of the respective ground state densities and the electron density (n_e) distribution. The latter is relatively flat within the core ($2 \leq z \leq 13$ mm) of the present C/H/O plasmas but declines as $z \to 0$ and (less steeply) at larger z.[1] Most of the input carbon in the hot region has been processed to CO, so the mole fraction X(CO) is also rather flat across this range. The CO number density is therefore lower where T_{gas} is greatest (i.e., $z \approx 10-12$ mm), while the H atom number density, from thermal dissociation of H_2, peaks in this region of highest T_{gas}. Thus, the CO* distribution peaks at smaller z than the H* distribution. The radical species most evident in emission are OH* (when $X_{C/\Sigma} < 0.5$) and CH*, C_2*, and C_3* (when $X_{C/\Sigma} > 0.5$). These species are each predicted to be concentrated in and around the hot plasma at the $X_{C/\Sigma}$ values of interest, as discussed in the companion article.[1]

Inspection of the data in Figure 2 reveals an apparent inconsistency. We have argued previously, in the context of C/H/Ar plasmas,[6] that the H* emission profiles provide the best visualization of the n_e distribution (i.e., the size of the plasma). Thus, the OES data displayed in Figure 2 imply that the n_e distribution in the present $CH_4/CO_2/H_2$ plasmas extends to $z \approx 20$ mm. This accords with the 2-D model, which assumes a cylindrical core of MW power absorption of height $H_{pl} \approx 16$ mm and radius $R_{pl} \approx 34$ mm for base conditions and a boundary region that decays over a few further mm. Yet the CH* and C_2* distributions, particularly those measured at $X_{C/\Sigma} \approx 0.5$, clearly stretch to considerably larger z. The observed profiles and trends are discussed in sections 3.5 and 3.6.

3.2. Optical Emission Profiles from C/H/O Plasmas at $X_{C/\Sigma} \approx 0.5$ as Functions of $X_0(H_2)$. The solid symbols in Figure 3 show the measured z-dependencies of (a) H(n = 3)* (the profiles for H(n = 4)* are essentially identical), (b) CO*, (c) OH*, (d) CH*, and (e) C_2* emissions from $CH_4/CO_2/H_2$ plasmas operating with $X_{C/\Sigma} = 0.495$ (to allow observation of OH* emission) and three different H_2 input mole fractions: $X_0(H_2) = 0.3$, 0.6, and 0.95. The relative intensities in each plot have been scaled so that the peak signal from the base ($X_0(H_2) = 0.3$) mixture is unity. The H elemental fractions in these three gas mixtures are X_{elem}(H) = 0.588, 0.714, and 0.952, and this scaling is partially reflected in the observed H* emission intensities, although many other factors (e.g., maximal T_{gas}, H(n = 1) concentration, T_e, etc.), which change upon varying X_{elem}(H) also affect the steady-state concentration of H* and the intensity of its emission. The CO* signal at $X_0(H_2) = 0.95$ is small, unsurprisingly, since the mole fraction X(CO) cannot exceed 0.05, but increases as $X_0(H_2)$ is reduced and, as in Figure 2, peaks at small z (∼5 mm). The shapes of the H*, CO*, and OH* profiles show no obvious sensitivity to $X_0(H_2)$, whereas the CH* and C_2* profiles clearly do. The latter both increase as $X_0(H_2)$ is reduced from 0.95 to 0.6, consistent with the increasing C fraction in the gas mixture (X_{elem}(C) rises from 0.024 versus 0.143), but then declines as $X_0(H_2)$ is further reduced to 0.3 (when X_{elem}(C) = 0.206). Additionally, their shapes change: the peaks of both distributions shift to smaller z and the relative intensities of the CH* and C_2* emissions at large z increase upon reducing $X_0(H_2)$. We return to consider these shifts, trends, and the evident expansion of the CH* and C_2* profiles (cf. those of H*, OH*, and CO*) in sections 3.5 and 3.6.

The open symbols in Figure 3a,b,d,e show the spatially resolved relative emission intensities of H(n = 3)*, CO*, CH*, and C_2* from the base CO/H_2 mixture measured under the same p, P, and detection conditions. Any OH* emission was too weak to recognize within the overlapping CO* emission. In plotting these data, each intensity has been scaled relative to that from a $CH_4/CO_2/H_2$ mixture with $X_{C/\Sigma} = 0.5$ and $X_0(H_2) = 0.3$ (i.e., with the exact same X_{elem}(C), X_{elem}(O), and X_{elem}(H)). Clearly, the emission profiles from the two source

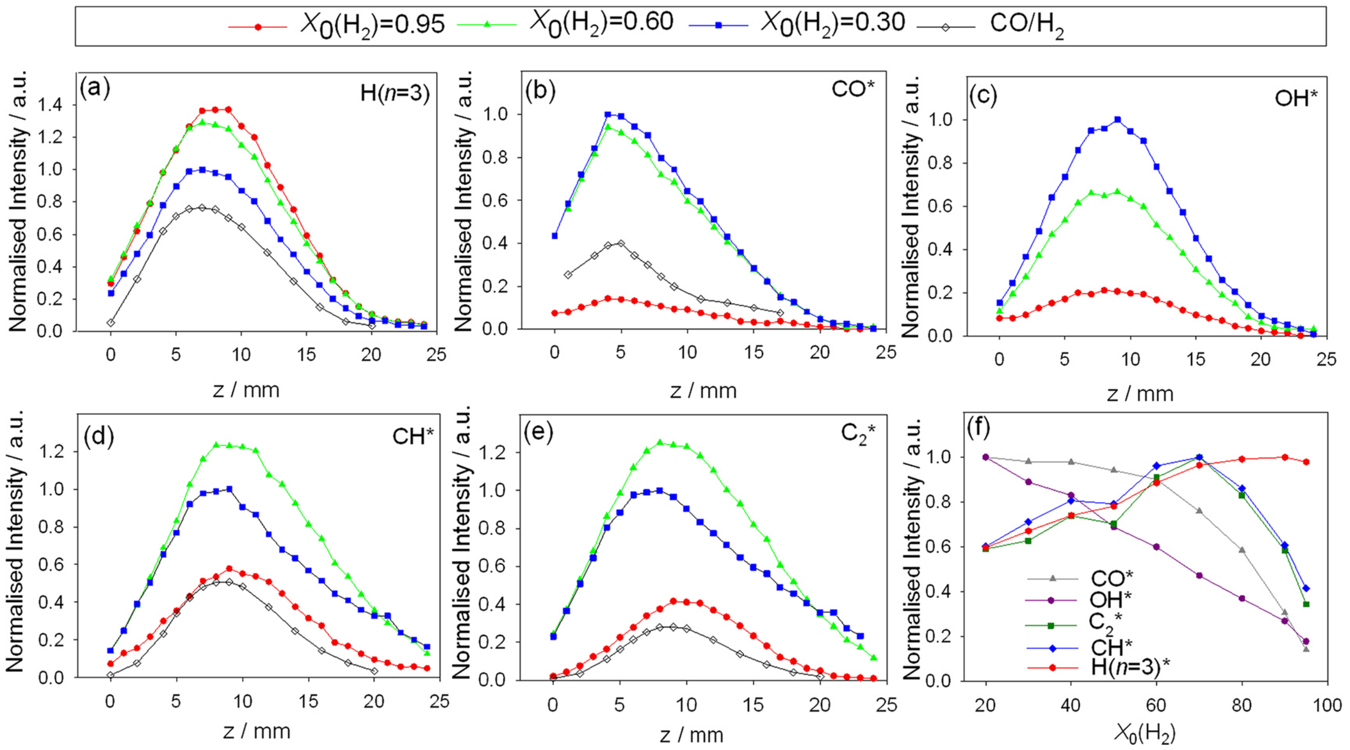

Figure 3. Spatial profiles (intensity versus z) of (a) H(n = 3)*, (b) CO*, (c) OH*, (d) CH*, and (e) C_2* emissions measured for $CH_4/CO_2/H_2$ plasmas with $X_{C/\Sigma} = 0.495$ and $X_0(H_2)$ = 0.3, 0.6, and 0.95 (filled symbols), and for a 41.2% CO/58.8% H_2 plasma (open symbols) each operating at base p and P. The data for the $CH_4/CO_2/H_2$ plasma within each panel are displayed on a common intensity scale, with the peak value for the $X_0(H_2)$ = 0.3 mixture set to unity; the CO/H_2 data in panels a, b, d, and e are scaled relative to that for a $CH_4/CO_2/H_2$ plasma with $X_{C/\Sigma}$ = 0.5 and $X_0(H_2)$ = 0.3. Panel f shows the way in which the intensity of each emitter measured from the $CH_4/CO_2/H_2$ plasmas at z = 10 mm varies with changes in $X_0(H_2)$ with, in this case, the maximum intensity of each emitter normalized to unity.

gas mixtures are similar, but those from the CO/H_2 mixture are consistently less intense. The H* intensity is reduced by ~25%, the CO* and CH* intensities are reduced ~2-fold, and the C_2* intensity is reduced at least 3-fold. OH* emission is very hard to identify from either $X_{C/\Sigma}$ = 0.5 plasma.

Figure 3f provides an alternative view of the way the various emission intensities from the $CH_4/CO_2/H_2$ mixtures with $X_{C/\Sigma}$ = 0.495 (measured at z = 10 mm) vary with $X_0(H_2)$. Decreasing $X_0(H_2)$ from 0.95 to 0.2 causes a concomitant increase in $X_{elem}(C)$ and $X_{elem}(O)$, from 0.024 to 0.222, and thus in the maximum possible CO mole fraction in the plasma ball (from 0.048 to 0.444). The measured CO* signal scales with the maximal $X(CO)$ value at high $X_0(H_2)$ (i.e., over the range 0.95 $\geq X_0(H_2) \geq$ 0.70), but levels off upon reducing $X_0(H_2)$ further. The intensities of all electron impact induced emissions are sensitively dependent upon the electron temperature, T_e. The observed trend in CO* emission intensities suggests that T_e is relatively constant at high $X_0(H_2)$, as found in our previous studies of C/H/Ar plasmas,[19] but declines as $X_0(H_2)$ is reduced further. Support for this conclusion is provided by the observed trends in emission intensities and by the 2-D modeling. The H content in the input gas mixture decreases almost 2-fold as $X_0(H_2)$ is reduced from 1.0 to 0.2, but the companion CRDS measurements[1] reveal a much smaller change in {H(n = 2)} over this range. This can be understood by the increase in the maximum T_{gas}, from ~2800 K to ~3000 K, and thus in the degree of H_2 dissociation, upon reducing $X_0(H_2)$. The companion 2-D modeling returns maximal hydrogen mole fractions $X(H)$ = ~0.05 at $X_0(H_2)$ = 0.95 and ~0.08−0.1 at $X_0(H_2)$ = 0.3, for p = 150 Torr and P = 1 kW.[1] Given the modest measured variation in {H(n = 2)}, the observed decline in H_α and, particularly, H_β emission intensities is most sensibly attributed to a reduction in T_e upon reducing $X_0(H_2)$, a view supported by the companion modeling, which suggests that T_e drops from ~1.15 eV to ~1.06 eV across the range covered in Figure 3f. The CRDS measurements also show that both {CH(X)} and {C_2(a)} increase when reducing $X_0(H_2)$, consistent with the increasing C fraction in the input gas mixture. The CH* and C_2* emission intensities also increase as $X_0(H_2)$ is reduced to ~0.7 but then fall if $X_0(H_2)$ is reduced further. Contributory reasons for this behavior are discussed in section 3.5.

OH* increases >5-fold upon decreasing $X_0(H_2)$ from 0.95 to 0.2. The companion CRDS measurements reveal a ~2-fold increase in {OH(X)} across this range, matching expectations based on the equilibrium

$$OH + H_2 \leftrightarrow H_2O + H \tag{1}$$

which implies

$$[OH] \approx \frac{[H]}{[H_2]}[H_2O] \tag{2}$$

and that [OH] should indeed increase with [H]/[H_2] ratio and with maximal [H_2O] upon decreasing $X_0(H_2)$, but if the CRDS measurements only show a 2-fold increase across the range and T_e decreases, we might expect a <2-fold increase in OH*, rather than the >5-fold increase that is actually observed. This finding points to the fact that the OH* observed by OES (and thus representative of OH in the plasma region) is only a fraction of the total OH column monitored by CRDS, as discussed in more detail in section 3.5.

3.3. $X_{C/\Sigma}$ Dependence of Optical Emission Intensities from C/H/O Plasmas. Figure 4 shows the variation in the optical emission intensities of H*, CO*, OH*, CH*, C_2*, and C_3* from $CH_4/CO_2/H_2$ plasmas upon tuning the gas composition through $X_{C/\Sigma} = 0.5$ at $X_0(H_2)$ = (a) 0.3, (b) 0.6, and (c) 0.95, while panel d shows the analogous plot obtained when progressively replacing up to 30 sccm of the CO flow in the base CO/H_2 plasma by CH_4 (i.e. $0.5 \leq X_{C/\Sigma} \leq 0.54$ at $X_0(H_2) = 0.588$). All data were measured at z = 10 mm, and the peak intensity of each emitter in each plot has been scaled to unity.

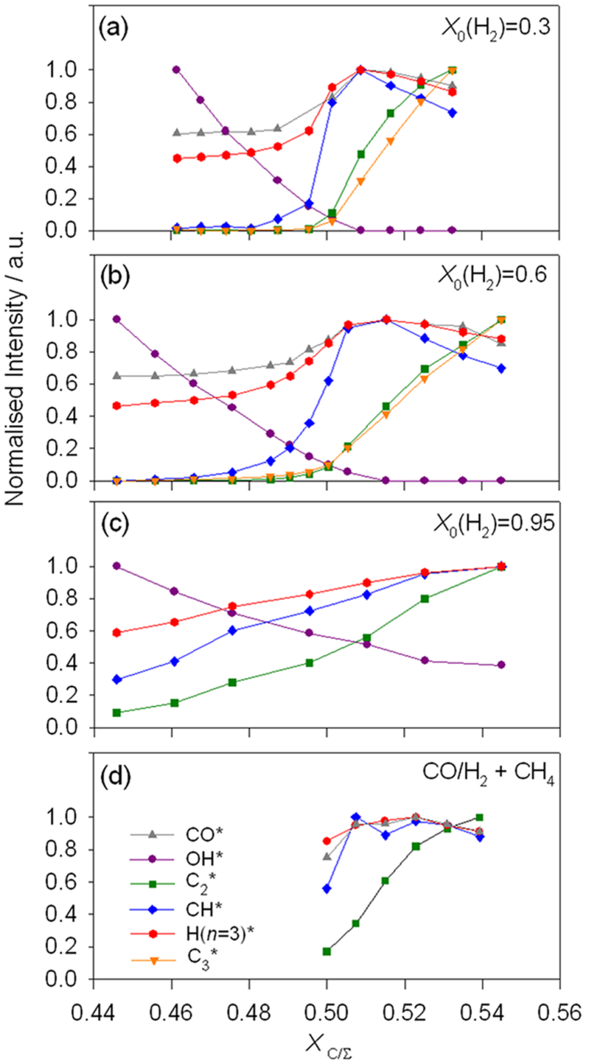

Figure 4. H(n = 3)*, CO*, OH*, CH* C_2*, and C_3* emission intensities from $CH_4/CO_2/H_2$ plasmas operating at base p and P, measured as a function of $X_{C/\Sigma}$ (at z = 10 mm) with $X_0(H_2)$ = (a) 0.3, (b) 0.6, and (c) 0.95. Panel d shows corresponding data starting from the 41.2% CO/58.8% H_2 plasma and tuning $X_{C/\Sigma}$ by progressively replacing CO with CH_4. The peak intensity of each emitter in each plot has been scaled to unity.

Figure 4a serves to quantify the trend evident from Figure 2. OH* falls with increasing $X_{C/\Sigma}$ and is barely discernible once $X_{C/\Sigma} = 0.5$. Conversely, the CH* emission intensity shows a step increase upon passing through $X_{C/\Sigma} \approx 0.5$ but eventually declines as $X_{C/\Sigma}$ is increased further. The H* and CO* emissions also show a (small) step increase at $X_{C/\Sigma}$ ~0.5, while the C_2* and C_3* emissions takeoff once $X_{C/\Sigma} > 0.5$. With the switch in dominant radical emitter, from OH* to CH*, C_2* (and C_3*) upon tuning through $X_{C/\Sigma} = 0.5$ broadly parallels the trends identified in CRDS measurements of the H(n = 2), OH(X), CH(X), and C_2(a) column densities and the 2-D plasma modeling.[1]

Measurements of $CH_4/CO_2/H_2$ plasmas with $X_0(H_2) = 0.6$ show a similar switch in emission character around $X_{C/\Sigma} = 0.5$ (Figure 4b), but this is progressively washed out upon further increases in $X_0(H_2)$ such that, by the time $X_0(H_2) = 0.95$ (Figure 4c), one simply sees a smooth decline in OH*, and smooth increases in CH* and, particularly, C_2* and C_3* across the range $0.45 \leq X_{C/\Sigma} \leq 0.55$.

Progressive replacement of CO by CH_4 in the CO/H_2 plasma (Figure 4d) results in similar variations in the emission intensities. This substitution only explores the $X_{C/\Sigma} > 0.5$ region, and OH* emission was not discernible within the overlapping CO* emission, but the data again shows an immediate increase in CH* emission and a more gradual increase in C_2* emission upon increasing $X_{C/\Sigma}$.

3.4. Variations of OES Intensities from $CH_4/CO_2/H_2$ Plasmas at $X_{C/\Sigma} = 0.495$, $X_0(H_2) = 0.3$, with Pressure and Power. Figure 5 displays the measured z-dependencies of the H*, CO*, OH*, CH*, and C_2* emission intensities measured at (a) 100 and (b) 200 Torr, with the peak of each profile normalized to unity. As in Figure 2, the CO* emission peaks at the smallest z, followed by the H* emissions, and the radical emissions are most extensive. The increased spatial extent of the CH* and C_2* emissions at lower p is noteworthy and will be considered further in section 3.5. Figure 5c shows how the relative intensities of each of these emissions (measured at z = 10 mm) varies across this pressure range. Doubling p (and thus the total number density) causes a drop in the measured H*, CO*, CH*, and C_2* emission intensities but an increase in OH* intensity. As always with OES, these changes are a reflection of changes in both the relevant species density and the electron distribution within the chosen viewing volume.

Detailed interpretation thus requires recourse to the companion CRDS measurements and the 2-D modeling. CRDS reveals a ~2-fold drop in {H(n = 2)} upon doubling p, a ~3-fold increase in {C_2(a)}, and little change in {CH(X)} or {OH(X)}.[1] The overall plasma volume decreases on increasing p. The total H atom density, [H], in the hot region is largely determined by the reaction

$$H_2 + M \rightarrow H + H + M \quad (M = H_2, CO_2, \text{etc.}) \tag{3}$$

or, in the case that M = CO, by a two-step reaction sequence.[1] [H] might thus be expected to at least double on doubling p; this increase will be further boosted by the inverse pressure dependence of the diffusion rate out of the hot region. Yet {H(n = 2)} and the H* emission intensities are both seen to fall. This difference reflects a drop in the EIE efficiency (EIEE), which scales as $\exp(-E'/T_e)$, where E' is the excited state energy (12.09 eV for H(n = 3)) and T_e is the electron temperature (in eV). The plasma modeling[1] returns $T_e \approx 1.06$ eV under base conditions (p = 150 Torr). A 2-fold change in EIEE for the H($n = 3 \leftarrow n = 1$) transition upon increasing/decreasing p by 50 Torr implies a 0.1 eV decrease/increase in T_e. X(CO) in the hot region is insensitive to p, so [CO] can be expected to scale with p. Thus, the observed fall in CO(b)* and CO(B)* emissions ($E' \approx 10.39$ and ~10.78 eV, respectively) with increasing p is also consistent with the deduced drop in T_e.

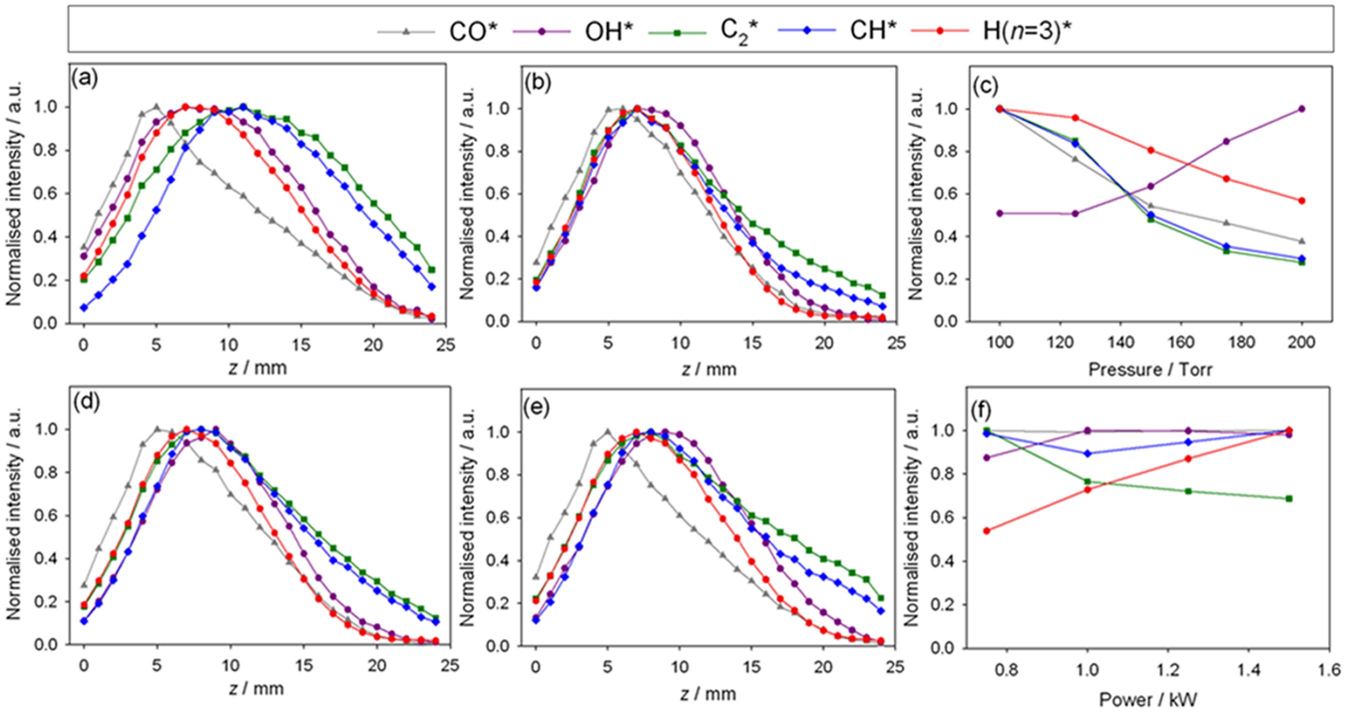

Figure 5. Spatial profiles (intensity versus z) of H(n = 3)*, CO*, OH*, CH*, and C_2* emissions measured for $CH_4/CO_2/H_2$ plasmas operating at base P with $X_{C/\Sigma}$ = 0.495 and $X_0(H_2)$ = 0.3 at p = (a) 100 and (b) 200 Torr. Each profile is displayed with the peak value set to unity. Panel c shows the variation of each emission intensity (measured at z = 10 mm) across the range $100 \le p \le 200$ Torr, with the maximum intensity of each emitter in this case shown as unity. Panels d and e show spatial profiles of the same emissions from $CH_4/CO_2/H_2$ plasmas operating at base p with $X_{C/\Sigma}$ = 0.495, $X_0(H_2)$ = 0.3, and P = 0.75 and 1.25 kW, respectively. Again, each profile is displayed with its peak value set to unity. Panel f shows how each emission intensity (at z = 10 mm) varies across the range $0.75 \le P \le 1.45$ kW, with the maximum intensity of each emitter again scaled to unity.

The p-dependence of the OH*, CH*, and C_2* emissions is more revealing. For example, CRDS shows little change in {OH(X)} but a ∼4-fold increase in {C_2(a)} at z = 10 mm upon increasing p from 100 to 200 Torr. Given the deduced drop in T_e, the EIEEs for forming OH* (E' = 4.02 eV) and C_2* (E' = 2.5 eV) should fall by factors of, respectively, 2 and 1.5 for this increase in p. Given these trends in column density and EIEE, we should expect a ∼2-fold decrease in OH* and a ∼2.6-fold increase in the C_2* emission intensity upon raising p from 100 to 200 Torr. In practice, we observe the reverse: OH* doubles and C_2* decreases more than 2-fold. Once again, these observations highlight the facts that (i) the spatial distributions of these radical species are extensive and inhomogeneous and that OES is biased in favor of the part of the total radical column density that overlaps best with the n_e profile, and (ii) sources other than EIE can contribute to the detected emission (as discussed in sections 3.5 and 3.6).

Figure 5d,e shows the measured z-dependencies of the H*, CO*, OH*, CH*, and C_2* emission intensities measured for base conditions and input powers P = 0.75 and 1.25 kW, respectively, with the peak of each profile normalized to unity. The various spatial profiles appear insensitive to this variation in P, and again, the CH* and C_2* emissions extend to the largest z. Figure 5f shows the variation in relative intensity of each of these emissions (measured at z = 10 mm) across the range $0.75 \le P \le 1.45$ kW. The most obvious effects of a near doubling of P are a ∼2-fold increase in H* and a ∼30% decrease in C_2* emission. Such behavior contrasts with that reported for dilute C/H/Ar plasmas,[6] wherein doubling P caused large (3- to 10-fold) increases in H*, CH*, and C_2* emission intensity, effects attributable to increases in n_e and in [H]/[H_2] ratio. The companion CRDS measurements of the $CH_4/CO_2/H_2$ plasma show a ∼2-fold increase in {H(n = 2)} upon doubling P, broadly consistent with the OES observations, increases in {CH(X)} and, particularly {C_2(a)}, and a ∼2-fold drop in {OH(X)}. Again, comparing the differing trends in radical density implied by OES with the absolute column densities returned by CRDS serves to highlight the differing extents of overlap between the radical and electron density distributions and/or the contributions of mechanisms other than EIE as sources of the observed emissions.

3.5. Plasma Parameters and Excited Species Behaviors Returned by the 2-D Model.

Understanding and explaining the wealth of OES (and CRDS) measurements tracking the spatially resolved behavior of several different species as functions of reactor parameters, in a range of C/H/O mixtures, is a challenge and a key aim of the 2-D modeling. The species emissions in the present MW plasma are (typically) pumped by EIE and depend on various coupling factors and processes: e.g., the plasma-chemical and electron kinetics, the electron concentration $n_e(r,z)$ and temperature $T_e(r,z)$, species concentrations, and the gas temperature $T_{gas}(r,z)$. Deriving a coherent, spatially resolved picture of the species emissions in the present work is further complicated by the 2-D/3-D discrepancies arising by the differences in the way gas enters the reactor experimentally (via two diametrically opposed 1/4″ pipes) and in the model (via a cylindrical ring), as discussed in the companion article.[1] These discrepancies have a serious effect on the various H_xO and C_xH_y densities calculated for base conditions ($X_0(H_2)$ = 0.3), a lesser (but still significant) impact on the calculated electron and ions densities, but little consequence for the calculated H atom, H_2, and CO concentrations. The sensitivity to source gas inlet geometry decreases with increasing $X_0(H_2)$ in $CH_4/CO_2/H_2$ mixtures (the measured and model results agree best in the case that $X_0(H_2)$ = 0.95) and should not be an issue for CO/H_2 mixtures. We can anticipate that all of these complications will apply to the respective excited species also.

3.5.1. Behavior of Emitting Species with Variations in $X_0(H_2)$. The way the various plasma parameters vary with changes in $X_0(H_2)$ was discussed in detail in ref 1, where the combined experimental and model study revealed the following trends with increasing $X_0(H_2)$ from 0.3 (base conditions, $X_{C/\Sigma}$ = 0.5) to 0.95: the plasma volume shrinks (from V = ~60 to ~35 cm^3), the respective power densities increase accordingly, the maximal n_e increases (from ~1.4 × 10^{11} to ~3 × 10^{11} cm^{-3}), as does T_e (from ~1.06 to ~1.15 eV), while the maximal T_{gas} and $X(H)$ decline from ~3000 to ~2815 K and from ~0.09 to ~0.05, respectively. Increasing $X_0(H_2)$ from 0.3 to 0.95 decreases $X_{elem}(C)$ and $X_{elem}(O)$, from 0.206 to 0.024. A detailed description of the effects of varying $X_0(H_2)$ on the spatial processing of the CH_4 and CO_2 source gases was presented in the companion article.[1] Briefly, the mutual destruction of H_xO and C_xH_y species within the smaller plasma volume at $X_0(H_2)$ = 0.95 is far from complete, and {CH} and {OH} thus increase less than proportionally with $X_{elem}(C)$ and $X_{elem}(O)$ as $X_0(H_2)$ is reduced. {C_2(a)}, in contrast, increases steeply upon reducing $X_0(H_2)$, reflecting the progressive increase in T_{gas} and [H].

All these factors will also affect the OH*, CH*, C_2*, H*, etc., emission intensities upon varying $X_0(H_2)$. The fall in T_e, from ~1.15 eV at $X_0(H_2)$ = 0.95 to ~1.06 eV at $X_0(H_2)$ = 0.3, is not particularly important for low lying excited states of OH*, CH*, and C_2* ($E' < 4.05$ eV) and will cause only limited (~15%) changes in EIE rates (cf., the >70% variations for CO(B or b) or H(n = 2, 3) emissions ($E' \geq 10.2$ eV)). The complex effects of all these factors and of changes in the source gas composition are illustrated in Figure 6, which shows z-profiles of the calculated column densities of H(n = 3) atoms and metastable CO($a^3\Pi$) molecules in $CH_4/CO_2/H_2$ mixtures with $X_0(H_2)$ = 0.3, $X_{C/\Sigma}$ = 0.5, with $X_0(H_2)$ = 0.95, $X_{C/\Sigma}$ = 0.505, and in the 41.2% CO/58.8% H_2 mixture. The concentration of metastable CO(a) molecules (E' = 6.04 eV) is determined by the balance between the rates of production (by EIE) and quenching, with CO and H_2.[1] The production rates (and column densities) of CO(a) and CO(b) have broadly similar profiles, peaking relatively nearer to the substrate. The calculated profiles of both CO(b) and H* and their calculated variations with process conditions, agree well with the respective OES data (Figure 3) and with the CRDS data for H(n = 2) (ref 1).

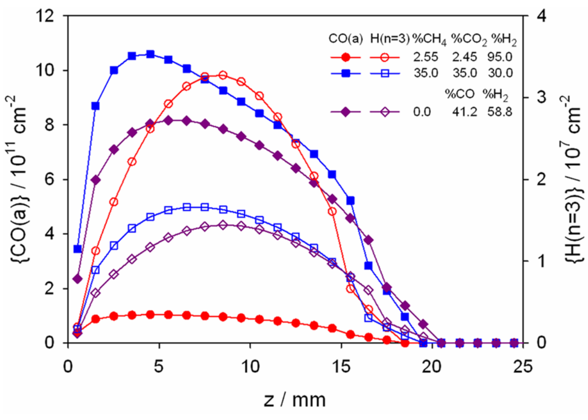

Figure 6. Spatial column density distributions of CO($a^3\Pi$) (left-hand axis, solid symbols) and H(n = 3) (right-hand axis, open symbols) predicted by the 2-D modeling of two $CH_4/CO_2/H_2$ mixtures with $X_0(H_2)$ = 0.95, $X_{C/\Sigma}$ = 0.505 and $X_0(H_2)$ = 0.3, $X_{C/\Sigma}$ = 0.5, and of the 41.2% CO/58.8% H_2 mixture.

Changes in the plasma parameters as a result of changes in process conditions are not the only factor affecting the emission from species like OH*, CH*, and C_2*. Obviously, their emission intensities will also depend on the extent of spatial overlap between the relevant parent species number density and the n_e distribution. This can be a sensitive function of, for example, $X_0(H_2)$, as can be seen by comparing the calculated [OH] and n_e distributions at $X_0(H_2)$ = 0.95, $X_{C/\Sigma}$ = 0.505 (Figure 7) with those for the base mixture ($X_0(H_2)$ = 0.3, $X_{C/\Sigma}$ = 0.5) shown in Figures 7 and 10b of ref 1. The spatial distributions of [CH], [C_2], and [OH] at $X_0(H_2)$ = 0.95 are all ball-like, irrespective of the detailed composition (in the range $0.46 \leq X_{C/\Sigma} \leq 0.54$, at least) and similar to those in the C/H plasmas studied previously.[20] This shape reflects the hottest region (peaking at r = 0) and deviates from that of the plasma volume only at larger z. A very different radial overlap is predicted for the base ($X_0(H_2)$ = 0.3, $X_{C/\Sigma}$ = 0.5) mixture, however. The calculated n_e distribution in this case exhibits a local maximum far from the plasma center, i.e., at $r \approx 2$ cm, while the OH(X), CH(X), and C_2(a) radical densities are predicted to maximize around the plasma edge.[1] Thus, we can trace a progressive shift in the region of maximal n_e from r = 0 to $r \approx 2$ cm as $X_0(H_2)$ is reduced from 0.95 to 0.3, during which its value falls from ~3 × 10^{11} to ~1.4 × 10^{11} cm^{-3}. The radical density distributions (at z = 10 mm) also evolve; the maximal [OH(X)] and [CH(X)] shift from r = 0 to $r \approx 3.5$ cm and $r \approx 3$ cm, respectively, with this decrease in $X_0(H_2)$.[1] Thus, we can anticipate that the optimal overlap between the n_e and [OH(X)] (and [CH(X)], [C_2(a)], etc.) distributions in (r,z) space, and thus, the OH*, CH*, C_2*, etc., OES intensities should be $X_0(H_2)$-dependent. The OES data in Figure 3 suggest that optimal overlap of the n_e and [CH(X)] (and [C_2(a)]) distributions (at z = 10 mm) is realized at $X_0(H_2)$ < 0.7.

The calculated CH* and C_2* profiles are in qualitative accord with the experimental data, but the correlation between the measured and calculated OH* profiles, and their variation with changes in process condition, is poor. The calculated spatial distributions of [OH(X)] and [CH(X)] are very similar at high $X_0(H_2)$ but differ significantly at base $X_0(H_2)$ = 0.3.[1] As Figure 3c,f shows, the OH* signal at z = 10 mm increases steadily (by a factor of ~4.5) upon reducing $X_0(H_2)$ from 0.95 to 0.3, despite the simultaneous decline in the calculated maximal n_e, in marked contrast to the calculated ~3-fold decrease in the EIE probability of OH(X) in the plasma region. Such a serious (order of magnitude) discrepancy might indicate the existence of other significant sources of OH* emission, in addition to EIE.

Thus, we have searched for other possible processes of OH* production, e.g., photodissociation of H_2O by Lyman-α emission from H(n = 2) atoms or photoexcitation of OH(X) by absorption of CO(b–a) emission. Even if they exist, neither process is able to reproduce the different observed versus predicted trends in OH* emission intensity. The CO(b–a) emission intensity increases upon reducing $X_0(H_2)$ from 0.95 to 0.3, even though T_e is deduced to decline. Thus, we might

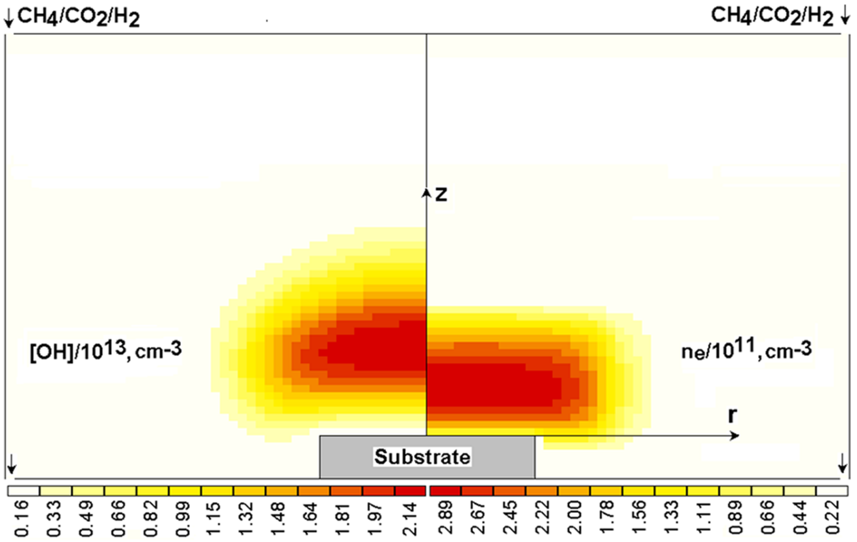

Figure 7. Calculated 2-D (r,z) number density distributions of OH(X) and n_e in a $CH_4/CO_2/H_2$ plasma operating under base reactor parameters (p = 150 Torr and P = 1 kW) and $X_0(H_2)$ = 0.95, $X_{C/\Sigma}$ = 0.505. Given the assumed cylindrical symmetry, only half (in the radial direction) of each 2-D distribution is displayed.

expect even greater relative increases in the concentrations of lower lying excited states of CO. This encouraged us to consider excitation transfer reactions involving such states of CO, most notably the metastable CO(a) state, and whether, for example, the known excitation transfer reaction 4 might become an increasingly important source of OH* emission upon reducing $X_0(H_2)$ in the present experiments:

$$CO(a^3\Pi) + OH(X^2\Pi) \rightarrow CO(X^1\Sigma^+) + OH(A^2\Sigma^+) \qquad (4)$$

The present reactor modeling[1] suggests that >15% of the absorbed MW power is expended on $CO(X^1\Sigma^+) \rightarrow CO(a^3\Pi)$ excitation, for which we assume an EIE coefficient $k_{(CO(X)\rightarrow CO(a))} = 4 \times 10^{-8} \exp(-6.04\ \mathrm{eV}/T_e)\ \mathrm{cm^3\ s^{-1}}$ at base conditions (calculated from the EIE cross-section data reported by Land[21]). Given the reported rate constant $k_4 = 4 \times 10^{-11}$ $\mathrm{cm^3\ s^{-1}}$ (ref 22), the 2-D model calculations show that this source will be quite efficient under the prevailing plasma conditions and, as a source of OH(A) radicals, could be of comparable (or even larger) importance than direct EIE of OH(X).

Figure 8 shows predicted axial profiles of this source and of other column production rates {R*} of OH*, CH*, and C_2* for two $CH_4/CO_2/H_2$ mixtures, with $X_0(H_2)$ = 0.3, $X_{C/\Sigma}$ = 0.5 and $X_0(H_2)$ = 0.95, $X_{C/\Sigma}$ = 0.505, and for a 41.2% CO/58.8% H_2 mixture at base reactor conditions. The column production rate {R*} = $\int R(r,z)\mathrm{d}r$ is defined as the radially integrated source of excited species due to, for example, electron excitation (e.g., OH(X, v = 0) + e → OH(A, v = 0) + e, labeled EIE(OH), for which $R(r,z) = k(T_e) \times n_e \times$ [OH(X, v = 0)]), excitation transfer (e.g., ET(CO(a) → OH(A)), for which R* is the rate of reaction 4) and various chemiluminescent (CL) reactions for CH* and C_2*. The observations (Figure 3) that the CH* and C_2* emission profiles broaden and that their maxima shift to larger z upon increasing $X_0(H_2)$, whereas those of H*, OH*, and CO(b) do not, provide further (indirect) evidence for nonplasma contributions to the former emissions. Possible sources of CH* and C_2* chemiluminescence are discussed in section 3.6.

The sum of all sources {R*} for any given species j is proportional to the column density and the emission intensity of this excited species. The calculated CH* and C_2* profiles and trends with varying $X_0(H_2)$ shown in Figure 8 are in qualitative accord with the experimental data (Figure 3), but the ET(CO(a) → OH(A)) source is too low (and would need to be an order of magnitude larger) to reproduce the measured $X_0(H_2)$ dependence of the OH* emission intensity (Figure 3f). We can envisage a number of reasons why the ET(CO(a) → OH(A)) source might be underestimated in the present modeling. First, the EIE coefficient k(CO(X) → CO(a)) would be ~2 times larger if we used the alternative energy dependent cross-section proposed by Haddad et al. (which shows a resonance at $E \approx 6.3$ eV).[23] Second, the T_{gas} dependencies of k_4 and of the quenching coefficient k_q for the CO(a) + CO → CO(X, high v) + CO reaction (reaction (19) from ref 1) are unknown and might be significantly different at $T_{gas} \approx 3000$ K. Finally, we recognize the possibility of the reverse reaction yielding CO(a) molecules from collisions involving CO(X, high v) molecules in regions where the CO vibrational distribution is out of equilibrium (i.e., $T_{vib}(CO) > T_{gas}$), either as a result of CO* quenching reactions or from electron impact induced vibrational ($E \rightarrow V$) excitations. In any case, the $E \rightarrow T$ transfer reaction 19 in ref 1 and reaction 4 (above) will both ensure fast inter-conversion and a degree of dynamic equilibrium between the group of excited species CO(X, high v) ↔ $CO(a^3\Pi)$ ↔ $OH(A^2\Sigma^+)$.

3.5.2. $X_{C/\Sigma}$ Dependence of Emitting Species at $X_0(H_2)$ = 0.3.

The observed changes in OH*, CH*, C_2*, and H(n = 3)* emission intensities with variations in $X_{C/\Sigma}$ at base $X_0(H_2)$ = 0.3 are broadly consistent with the measured (by CRDS) behavior of ground state OH and CH, C_2(a), and H(n = 2), respectively.[1] However, the emitting species are sensitive to any changes in n_e and T_e since these affect the EIE efficiency, and such changes are invoked to account for the observed local maxima in the CH*, CO*, and H* emission intensities at $X_{C/\Sigma}$ ≈ 0.51 (Figure 4a).

Indeed, the 2-D model predicts a nonmonotonic variation in T_e with $X_{C/\Sigma}$ (1.0, 1.06, and 1.05 eV at $X_{C/\Sigma}$ = 0.47, 0.5, and 0.54, respectively) and substantial changes in the n_e distribution at $X_{C/\Sigma}$ ≈ 0.5 (where the maximum shifts toward the plasma edge) but with similar maximal n_e values [~(1.3−1.4) × 10^{11}

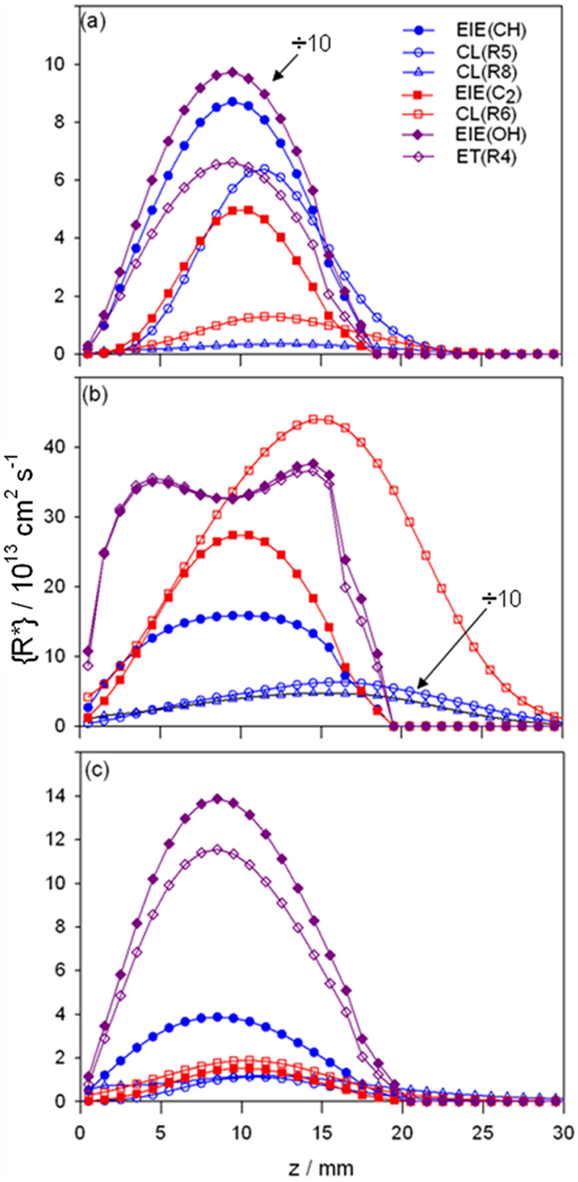

Figure 8. Predicted z-dependencies of the radially ($-R_r < r < R_r$) integrated products $\{R^*(z)\}=\{k_5^* \times [O] \times [C_2H]\}$, $\{k_8^* \times [C] \times [H] \times [M]\}$, and $\{k_{EIE} \times [CH(X, v = 0)] \times n_e\}$ (contributors to CH* emission), of the analogous quantities $\{k_6^* \times [C] \times [CH]\}$ and $\{k_{EIE} \times [C_2(a, v = 0)] \times n_e\}$ (contributors to C_2* emission), and of the EIE and ET($CO(a^3\Pi) \rightarrow OH(A^2\Sigma^+)$) contributions to OH* emission from three different C/H/O plasmas: (a) $CH_4/CO_2/H_2$ with $X_0(H_2) = 0.95$, $X_{C/\Sigma} = 0.505$, (b) $CH_4/CO_2/H_2$ with $X_0(H_2) = 0.3$, $X_{C/\Sigma} = 0.5$, and (c) 41.2% CO/58.8% H_2, each operating at base pressure p = 150 Torr and input power P = 1 kW. For ease of display, the $\{R^*\}$ values associated with one of the curves in each of panels a and b have been divided by 10 prior to plotting.

cm^{-3}] across this range of $X_{C/\Sigma}$. The changes in T_e and n_e across this $X_{C/\Sigma}$ range reflect two factors. First, the total ionization rate increases, as C_2H_2 ionization starts to contribute (at $X_{C/\Sigma} \approx 0.5$) and eventually dominates (by $X_{C/\Sigma} = 0.54$). Second, the electron-ion recombination rate increases, as the dominant ion evolves from H_3O^+ at $X_{C/\Sigma} = 0.47$, through a mixture of H_3O^+ and $C_xH_y^+$ at $X_{C/\Sigma} = 0.5$ to $C_xH_y^+$ ($X_{C/\Sigma} = 0.54$).[1] These effects act in tandem but show different dynamics with $X_{C/\Sigma}$. The 2-D model qualitatively reproduces the local maxima in the H(n = 3)* and CO* emission intensities vs $X_{C/\Sigma}$ plots at $X_0(H_2) = 0.3$ (Figure 4a): the calculated relative EIE rates collected for CO(b) and H(n = 3) at $z \approx 10$ mm and $X_{C/\Sigma}$ = 0.47, 0.5, and 0.54 are 0.85:1:0.92 and 0.71:1:0.81, respectively. The OH*, CH*, and C_2* emission intensities are obviously much more sensitive to these changes in $X_{C/\Sigma}$ because of the dramatic changes in the underpinning chemistry upon crossing the H−CO tie-line ($X_{C/\Sigma} = 0.5$). By way of comparison with the $X_0(H_2) = 0.3$ data shown in Figure 4a, the 2-D model returns the following relative EIE radially integrated rates at $X_{C/\Sigma}$ = 0.47, 0.5 and 0.54: OH*, 1:0.011:0.001; CH*, 0.024:0.8:1 and C_2*,: 0.0002:0.08:1.

When $X_0(H_2) = 0.95$, in contrast, we find no substantial changes in T_e (~1.15 eV), the n_e distribution (Figure 7), or in the ionization and electron-ion recombination rates within this range of $X_{C/\Sigma}$. C_2H_2 and H_2 ionization are the dominant contributions to the former rate, while the latter involves comparable contributions from the e + $C_xH_y^+$ and e + H_3O^+ recombination reactions (i.e., H_3O^+ is the dominant ion). As discussed previously,[1] the much reduced sensitivity to $X_{C/\Sigma}$ in the H_2-rich plasma (cf., $X_0(H_2) = 0.3$) reflects differences in the spatial processing of the CH_4 and CO_2 source gases and the less complete mutual conversion of C_xH_y and H_xO species into CO, which results in much smoother variations in C_xH_y and H_xO densities within the plasma region. Again, the predicted changes in species emissions due to EIE (collected at z = 10 mm) upon increasing $X_{C/\Sigma}$ from 0.505 to 0.54 (i.e., CO* and OH* decrease by, respectively, 8% and 21%, while H(n = 3)*, CH*, and C_2* increase by 3%, 6%, and 27%) are in very reasonable accord with the experimental observations (Figure 4c).

3.5.3. Effects of Pressure and Power Variations at $X_{C/\Sigma}$ = 0.5, $X_0(H_2)$ = 0.3.

To trace the effects of varying the total pressure and the applied MW power, additional 2-D model calculations were undertaken at p = 200 Torr (cf., 150 Torr) and P = 1.5 kW (cf., 1 kW) with all other parameters held at their base values ($X_{C/\Sigma} = 0.5$, $X_0(H_2) = 0.3$). The data in Figure 5f suggests only modest variations in the EIE rates (at z = 10 mm) upon increasing P from 1 to 1.5 kW: H(n = 3)* emissions increase ~30%, while OH*, CH*, and C_2* each change by <10%, implying that the plasma parameters (T_e, n_e), T_{gas}, X(H), etc., are little changed by this increase in P. The 2-D modeling shows that very similar plasma parameters and emission intensities would result if increasing P results in some reduction in the average power density, from $P/V \approx 17$ W cm^{-3} for the base P = 1 kW to $P/V \approx 13.5$ W cm^{-3} for P = 1.5 kW, implying that the plasma volume increases from $V \approx 60$ cm^3 under base conditions to $V \approx 110$ cm^3 at P = 1.5 kW. Given $V \approx 110$ cm^3, the calculated EIE rates for P = 1.5 kW (collected at z = 10 mm) show <10% increases in the cases of H(n = 3)*, CO*, and CH* and <20% increases for OH* and C_2*, relative to base conditions.

The monitored emissions show more variable dependencies on pressure (Figure 5c). All except OH* decrease with increasing p. The 2-D modeling focused particularly on reproducing the observed trends in CO(b)* and H(n = 3)* emissions since these species are least sensitive to the recognized shortcomings due to neglect of the azimuthal asymmetry of the input gas feed. For p = 200 Torr (and a sensibly reduced plasma volume $V \approx 53$ cm^3), the 2-D model returns the following plasma parameters: average $T_e \approx 1.04$ eV, maximal $n_e \approx 1.2 \times 10^{11}$ cm^{-3}, X(H) = 0.1, and $T_{gas} \approx 2960$ K. The EIE rates (at z = 10 mm) for forming CO*, OH*, CH*, and H(n = 3)* are all predicted to decline relative to those at p = 150 Torr (by 12%, 55%, 24%, and 10%, respectively), whereas the EIE rate for forming C_2* is predicted to increase by 19%. As with the $X_0(H_2)$ dependencies, EIE alone (i.e., without any allowance for ET(CO(a) → OH(A)) notably fails to reproduce the experimental trends in OH* emission intensity.

The contrasting p and P dependencies of the C_2 absorbance and C_2* emission intensities measured at $z = 10$ mm also merit comment; the absorbance (by CRDS) grows with increasing p and P (Figure 6 of ref 1), whereas the C_2* emission intensities fall. The 2-D modeling reproduces the observed anticorrelation in p, but not in P. The calculated column density increases with increasing p ($\{C_2(a, v = 0)\} = 3.2 \times 10^{12}$ cm^{-2} for $p = 200$ Torr; cf., 2.6×10^{12} cm^{-2} for $p = 150$ Torr), while the calculated C_2* emission intensity at 200 Torr is 17% lower than at 150 Torr. In the case of P, however, the model predicts increases in both $\{C_2(a, v = 0)\}$ and in the C_2* emission intensity (by EIE) upon raising P from 1 to 1.5 kW (by 37% and 19%, respectively). For both CH and H(n = 2, 3), the 2-D modeling returns trends in p and P that are consistent with both the CRDS and OES data. The present data highlights the potential pitfalls when comparing integrated EIE rates and OES intensities; such comparisons will inevitably fail in instances where alternative processes (e.g., excitation transfer processes, as invoked in the case of OH(A) excitation through collision with metastable CO(a) molecules, and CL reactions, as discussed below for the cases of C_2* and CH*) make comparable contributions to the measured emission intensities.

3.6. Contribution of Chemiluminescent Reactions to the Observed Emissions. CL reactions yielding species like OH*, CH*, and C_2* are important in hot C/H/O mixtures (i.e., flames),[24,25] and it is thus logical to consider the extent to which such reactions might supplement EIE as a source of optical emission from MW-activated C/H/O mixtures. The reaction of C_2H radicals with O atoms and/or O_2 molecules is a recognized route to CH* in flames, with lesser contributions from C_2 + OH. The low O_2 density in the hot region ensures that the $C_2H + O_2$ reaction will be unimportant in MW-activated C/H/O plasmas. Smith et al.[24] proposed a rate constant of 1.03×10^{-11} cm^3 s^{-1} for the reaction

$$C_2H + O \rightarrow CH^* + CO \qquad (5)$$

which, given the reactant densities predicted by the present 2-D modeling, would imply CH* densities in the base $CH_4/CO_2/H_2$ plasma stretching to z values well beyond those where there is any significant electron density. From our OES and 2-D model results (Figures 3 and 8), we derive and use a rate coefficient $k_5^* = 4.15 \times 10^{-12}$ cm^3 s^{-1} for forming CH*(v = 0). The recommended total rate coefficient for the C_2H + O reaction (i.e., for forming both CH(X) and CH* products) is $k_{5(tot)} = 8.3 \times 10^{-11}$ cm^3 s^{-1} (ref 26), thus implying a CL yield $k_5^*/k_{5(tot)} = 0.05$. The recognized discrepancy in the way the 2-D model approximates the asymmetric delivery of the source gas mixture results in serious overestimations of the concentrations of all C_2H_x species under base conditions; this effect is evident in Figure 8b, where the contribution from reaction 5 is plotted on a 10× reduced vertical scale.

As noted previously, the 2-D model reproduces the H_2-rich $CH_4/CO_2/H_2$ plasma and CO/H_2 plasma measurements more quantitatively, so we now focus on these plasmas to illustrate likely CL contributions to the measured optical emissions. Figure 8a shows the calculated spatially resolved CH* production rates from reaction 5 (and reaction 8, see below) and from EIE of CH(X) radicals in a $CH_4/CO_2/H_2$ plasma with $X_0(H_2) = 0.95$ and $X_{C/\Sigma} = 0.505$. The CH($A^2\Delta$, $v = 0 \leftarrow X^2\Pi$, $v = 0$) EIE cross-section data from Celiberto et al.[27] yields an EIE coefficient $k_{EIE}(CH) = 1.1 \times 10^{-9} \exp(-2.87\ \mathrm{eV}/T_e)$ cm^3 s^{-1} for the electron energy distribution appropriate to the H_2-rich plasma; for the 41.2% CO/58.8% H_2 mixture (and the base $CH_4/CO_2/H_2$ mixture), we use $k_{EIE}(CH) = 1.8 \times 10^{-9} \exp(-2.87\ \mathrm{eV}/T_e)$). For EIE of C_2 Swan band emission, we use $k_{EIE}(C_2) = 9.8 \times 10^{-9} \exp(-2.5\ \mathrm{eV}/T_e)$ for the H_2-rich plasma (as calculated for our previous analysis of H_2-rich C/H plasmas[19]) and $k_{EIE}(C_2) = 1.05 \times 10^{-8} \exp(-2.5\ \mathrm{eV}/T_e)$ cm^3 s^{-1} for the base mixture and the 41.2% CO/58.8% H_2 mixture. [For completeness, a rate coefficient for EIE of OH(X) was calculated assuming the same cross-section versus energy dependence as for CH, but with the threshold shifted from 2.87 to 4.05 eV (the OH(A–X) energy separation), giving $k_{EIE}(OH)$ values of, respectively, $1.6 \times 10^{-9} \exp(-4.05\ \mathrm{eV}/T_e)$ and $3 \times 10^{-9} \exp(-4.05\ \mathrm{eV}/T_e)$ cm^3 s^{-1} for $X_0(H_2) = 0.95$ and $X_0(H_2) = 0.3$]. We also note that, relative to reaction 5, the C_2 + OH → CH + CO reaction (with total rate coefficient $k = 1.9 \times 10^{-11}$ cm^3 s^{-1} and an assumed branching into CH* products $k^* < 0.05k$) is not a significant source of CH* chemiluminescence under the present conditions. As Figure 8 shows, the EIE and CL routes to CH* emission have clearly different spatial profiles under all process conditions, with the latter peaking at (and extending to) larger z. Equally clearly, a suitably weighted sum of the two could account for the extended distribution of CH* emissions observed not just under these H_2-rich conditions and in the CO/H_2 plasma (Figures 8a,b) but, accepting the previously noted discrepancy between measured and calculated C_xH_y and OH_x column densities at lower $X_0(H_2)$, for the base mixture also (Figure 8c).

The C_2* emission profiles (Figures 2b and 3e) show a similarly extended tail at large z. C_2* emission in flames is usually attributed to the radical–radical reaction[24]

$$C + CH \rightarrow C_2^* + H \qquad (6)$$

though reaction of C_3 radicals with O_2 has been proposed also.[28] Again, the low O_2 density in the hot plasma region ensures that the latter reaction will be unimportant in MW-activated C/H/O plasmas. The $C_3 + O \rightarrow C_2 + CO$ reaction is also sufficiently exothermic to yield C_2* products, but an unphysically large rate coefficient ($k^* \approx 2.5 \times 10^{-10}$ cm^3 s^{-1}) would be required in order for it to be comparable with the rate of reaction 6 for which we assume $k_6^* = 0.0075k_6 = 2.5 \times 10^{-12}$ cm^3 s^{-1}. The z-dependent column rates $\{k_6^* \times [C] \times [CH]\}$ predicted by the 2-D model for all conditions (Figure 8) clearly support the view that reaction 6 could account for the extended tail of C_2* emission from the present C/H/O plasmas. The spatial distribution of C_3* emission in carbon-rich $CH_4/CO_2/H_2$ plasmas is also seen to extend to large z (Figure 2c), and 2-D modeling identifies the CH + C_2 → C_3* + H reaction as a likely candidate for C_3* chemiluminescence.

The 2-D model also explains the observation that the tails of the CH* and C_2* emissions at large z are relatively greater at $X_{C/\Sigma} = 0.495$ than at 0.54 (cf., Figure 2b,c). The calculated distributions of C, CH, and C_2 concentration in the carbon-rich plasma ($X_{C/\Sigma} = 0.54$, $X_0(H_2) = 0.3$) are all ball-shaped, peaking at $r = 0$ and $z \approx 11$–12 mm[1] (reflecting the shape of the hot central region), so both the EIE and CL yields from this region of the plasma are enhanced relative to the CL-only contribution at the periphery.

OH* emission is seen in most combustion flames and normally attributed to reaction of CH radicals with O_2 and the association reaction O + H + M → OH* + M.[29] The calculated rates of both reactions in a MW-activated C/H/O plasma are much too low for either to be a significant source of OH* under base conditions, and consistent with this view, the spatial profiles of the OH* emissions measured in the present work (Figures 2b, 5, etc.) are generally consistent with pure plasma sources (i.e., EIE of OH(X) and ET(CO(a) → OH(A))).

We have previously reported[16] a halo of BH(A → X) emission following the addition of trace amounts of B_2H_6 to a MW-activated Ar/H_2 plasma; this violet emission appeared to fill the reactor and clearly extended to very large z. Given the apparent lack of alternatives, this was tentatively ascribed to EIE of BH(X) radical, the distribution of which was shown by CRDS and by modeling to extend to large z, even though the emission at the largest z emanated from regions where the model electron density had fallen to zero. The recognition that CL reactions make recognizable contributions to the CH* and C_2* emissions observed from C/H/O plasmas operating under a wide range of process conditions encourages a review of this interpretation. The recombination of ground state B and H atoms

$$B + H + M \rightarrow BH + M \tag{7}$$

is highly exothermic: $\Delta_r H \approx -3.6$ eV. These reactants correlate with ground ($X^1\Sigma^+$) and excited ($A^1\Pi$) state BH radicals via potentials that, in both cases, are essentially barrierless.[30] Revisiting the previous modeling of B/H/Ar plasma,[31] we find that the BH* column production rate in the case of a B/H/Ar plasma (i.e., the radially integrated product $\{k_7 \times [B] \times [H] \times [M]\}$, with $[M] = [H_2]$ and reaction coefficient $k_7 = 3 \times 10^{-33} \exp(-1000/T_{gas})$ cm^6 s^{-1}, from ref 32) peaks at $z \approx 30$ mm and is certainly sufficiently extensive to account for the observed halo that fills the whole reactor volume. The BH* emission from B/C/H/Ar plasmas was less extensive[33] but still extends to $z > 20$ mm where the companion modeling suggests negligible electron density. Again, it is clear that a suitably weighted sum of the calculated contributions of BH* chemiluminescence and EIE of BH(X) could offer a much more satisfactory explanation for the observed BH* emission profiles in both B/H/Ar and B/C/H/Ar plasmas.[34]

Having identified recombination of ground state atoms as a source of optical emission in MW-activated B/(C)/H/Ar plasmas, it is prudent to consider whether analogous reactions like

$$C + H + M \rightarrow CH(A) + M \quad \Delta_r H \approx -0.6 \text{ eV} \tag{8}$$

or

$$C + C + M \rightarrow C_2(d) + M \quad \Delta_r H \approx -3.7 \text{ eV} \tag{9}$$

might also contribute to the CH* and C_2* emissions observed, for example, in MW-activated C/H/Ar gas mixtures. Reactions 8 (which has also been proposed in the context of flames[24]) and 9 are sufficiently exothermic to form CH(A) and C_2(d) radicals, respectively. In both cases, the excited state of interest correlates diabatically with an excited C(^{1}D) atom, the relative abundance of which (at $T_e \approx 1$ eV) will be ~15% that of the ground state C(^{3}P) atoms. The present calculations show that reaction 8 with C(^{1}D) as reagent and an assumed value $k_8^* = 7 \times 10^{-31}/T_{gas}$ cm^6 s^{-1} (half of total rate coefficient for the reaction $O + H + M \rightarrow OH + M$) would contribute to emission at large z (Figure 8), though is likely to be relatively less important than reaction 5 in the present MW-activated C/H/O plasmas. We note that reaction 9 has previously been invoked as a major source of C_2(d → a) emission from a dc arc-jet plume but that CL reactions were deduced to make no significant contribution to the observed CH* emissions.[35] Our 2-D modeling of this arc-jet plume, however, suggests that reaction 8 could well provide a better correlation with the reported CH* emission map than any of the other CH* sources.

4. CONCLUSIONS

MW-activated $CH_4/CO_2/H_2$ and CO/H_2 plasmas operating under conditions relevant to diamond CVD have been investigated by OES and by detailed companion 2-D plasma modeling. Spatially resolved measurements of emissions from electronically excited H(n = 3) atoms, OH*, CH*, C_2* and C_3* radicals, and CO* molecules within the hot plasma region, as functions of process conditions (gas mixing ratio, P, and p), reveal a clear switch in plasma chemistry and composition upon changing from an oxygen-rich ($X_{C/\Sigma} < 0.5$) to a carbon-rich ($X_{C/\Sigma} > 0.5$) plasma, reinforcing the results of spatially resolved absorption measurements made under identical plasma conditions.[1] The 2-D modeling reveals different plasma-chemical activation mechanisms in $CH_4/CO_2/H_2$ and CO/H_2 mixtures, a hidden subtlety buried within the Bachmann diagram, that is indirectly confirmed by both the experimental OES and CRDS data.[1]

At a more detailed level, however, the present study identifies a number of complicating factors that need to be recognized in order for observed changes in OES intensity to be related to changes in the C/H/O plasma. OES data is traditionally interpreted on the basis that the emitting species of interest is formed by EIE of the corresponding ground state species. Yet, the OH* emission intensities from $CH_4/CO_2/H_2$ plasmas with $X_{C/\Sigma} \leq 0.5$ are often seen to be anticorrelated with the measured column densities of ground state OH(X) radical, a finding that can be traced to an alternative OH* production route, excitation energy transfer from metastable CO($a^3\Pi$) molecules in the hot plasma region. The CH* and C_2* emission profiles, particularly from gas mixtures with $X_{C/\Sigma} \approx 0.5$, are found to extend to z values where the electron density (required for EIE) has fallen to zero. Such emission at large z can be traced to chemiluminescent reactions between, for example, C_2H radicals and O atoms or C atoms and CH radicals. In hindsight, it is clear that chemiluminescent reactions are responsible for the extensive BH* emissions observed in our previous studies of B/H/Ar and B/C/H/Ar plasmas.[31,33,34] Finally, we note that the EIE efficiencies of each of the monitored radical species in a $CH_4/CO_2/H_2$ plasma are sensitive not just to the plasma parameters but also to any spatial mismatch between the regions of maximal radical and electron density, both of which are sensitive functions of $X_{C/\Sigma}$ when $X_{C/\Sigma} \approx 0.5$ (as required for diamond growth) and of the H_2 mole fraction.

■ AUTHOR INFORMATION

Corresponding Author

*Tel: (117) 9288312. Fax: (117) 9277985. E-mail: mike.ashfold@bris.ac.uk.

Notes

The authors declare no competing financial interest.

■ ACKNOWLEDGMENTS

The Bristol group is grateful to EPSRC for funding (grant no. EP/H043292/1), Element Six Ltd for financial support and the long term loan of the MW reactor, and colleagues K. N. Rosser, J. A. Smith, and S. C. Halliwell for their many contributions to the work described here. M.N.R.A. is also grateful to the Royal Society for the award of a Royal Society Leverhulme Trust Senior Research Fellowship.

REFERENCES

(1) Kelly, M. W.; Richley, J. C.; Western, C. M.; Ashfold, M. N. R.; Mankelevich, Y. A. *J. Phys. Chem. A* **2012**, DOI: 10.1021/jp306190n, companion article.

(2) Gicquel, A.; Hassouni, K.; Breton, Y.; Chenevier, M.; Cubertafon, J. C. *Diamond Relat. Mater.* **1996**, *5*, 366.

(3) Gicquel, A.; Derkaoui, N.; Rond, C.; Benedic, F.; Cicala, G.; Moneger, D.; Hassouni, K. *Chem. Phys.* **2012**, *398*, 239.

(4) Gicquel, A.; Hassouni, K.; Farhat, S.; Breton, Y.; Scott, C. D.; Lefebvre, M.; Pealat, M. *Diamond Relat. Mater.* **1994**, *3*, 581.

(5) Gicquel, A.; Chenevier, M.; Hassouni, K.; Tserepi, A.; Dubus, M. *J. Appl. Phys.* **1998**, *83*, 7504.

(6) Ma, J.; Ashfold, M. N. R.; Mankelevich, Y. A. *J. Appl. Phys.* **2009**, *105*, 043302.

(7) Gicquel, A.; Derkaoui, N.; Rond, C.; Benedic, F.; Cicala, G.; Moneger, D.; Hassouni, K. *Chem. Phys.* **2012**, *398*, 239.

(8) Kawato, T.; Kondo, K. *Jpn. J. Appl. Phys.* **1987**, *26*, 1429.

(9) Muranaka, Y.; Yamashita, H.; Sato, K.; Miyadera, H. *J. Appl. Phys.* **1990**, *67*, 6247.

(10) Balestrino, G.; Marinelli, M.; Milani, E.; Paoletti, A.; Pinter, I.; Tebano, A. *Appl. Phys. Lett.* **1993**, *62*, 879.

(11) Chen, C. F.; Chen, S.; Ko, H.; Hsu, S. E. *Diamond Relat. Mater.* **1994**, *3*, 443.

(12) Stiegler, J.; Lang, T.; Nygard-Ferguson, M.; von Kaenel, Y.; Blank, E. *Diamond Relat. Mater.* **1996**, *5*, 226.

(13) Elliott, M. A.; May, P. W.; Petherbridge, J. R.; Leeds, S. M.; Ashfold, M. N. R.; Wang, W. N. *Diamond Relat. Mater.* **2000**, *9*, 311.

(14) Petherbridge, J. R.; May, P. W.; Pearce, S. R. J.; Rosser, K. N.; Ashfold, M. N. R. *J. Appl. Phys.* **2001**, *89*, 1484.

(15) Mollart, T. P.; Lewis, K. L. *Diamond Relat. Mater.* **1999**, *8*, 236.

(16) Ma, J.; Richley, J. C.; Davies, D. R. W.; Cheesman, A.; Ashfold, M. N. R.; Mankelevich, Y. A. *J. Phys. Chem. A* **2010**, *114*, 2447.

(17) Ma, J.; Richley, J. C.; Ashfold, M. N. R.; Mankelevich, Y. A. *J. Appl. Phys.* **2008**, *104*, 103305.

(18) Bachmann, P. K.; Leers, D.; Lydtin, H. *Diamond Relat. Mater.* **1991**, *1*, 1.

(19) Richley, J. C.; Fox, O. J. L.; Ashfold, M. N. R.; Mankelevich, Y. A. *J. Appl. Phys.* **2011**, *109*, 063307.

(20) Mankelevich, Y. A.; Ashfold, M. N. R.; Ma, J. *J. Appl. Phys.* **2008**, *104*, 113304.

(21) Land, J. E. *J. Appl. Phys.* **1979**, *49*, 5716.

(22) Wategaonkar, S. J.; Setser, D. W. *J. Phys. Chem.* **1990**, *94*, 7200.

(23) Haddad, G. N.; Milloy, H. B. *Aust. J. Phys.* **1983**, *36*, 473.

(24) Smith, G. P.; Luque, J.; Park, C.; Jeffries, J. B.; Crosley, D. R. *Combust. Flame* **2002**, *131*, 59.

(25) Panoutsos, C. S.; Hardalupas, Y.; Taylor, A. M. K. P. *Combust. Flame* **2009**, *156*, 273.

(26) Smith, G. P.; Golden, D. M.; Frenklach, M.; Moriarty, N. W.; Eiteneer, B.; Goldenberg, M.; Bowman, C. T.; Hanson, R. K.; Song, C.; Gardiner, W. C., Jr.; Lissianski, V. V.; Qin, Z. GRI-Mech; see http://www.me.berkeley.edu/gri-mech.

(27) Celiberto, R.; Janev, R. K.; Reiter, D. *Plasma Phys. Controlled Fusion* **2009**, *51*, 085012.

(28) Mann, D. M. *Chem. Phys. Lett.* **1977**, *47*, 106.

(29) Hall, J. M.; Petersen, E. L. *Int. J. Chem. Kinet.* **2006**, *38*, 714.

(30) Petsalakis, I. D.; Theodorakopoulos, G. *Mol. Phys.* **2007**, *105*, 333.

(31) Ma, J.; Richley, J. C.; Davies, D. R. W.; Cheesman, A.; Ashfold, M. N. R.; Mankelevich, Y. A. *J. Phys. Chem. A* **2010**, *114*, 2447.

(32) Pasternack, L. *Combust. Flame* **1992**, *90*, 259.

(33) Ma, J.; Richley, J. C.; Davies, D. R. W.; Ashfold, M. N. R.; Mankelevich, Y. A. *J. Phys. Chem. A* **2010**, *114*, 10076.

(34) Ma. J. Ph.D. thesis, University of Bristol, 2008.

(35) Luque, J.; Juchmann, W.; Brinkman, E. A.; Jeffries, J. B. *J. Vac. Sci. Technol., A* **1998**, *16*, 397.